**Highlighting a study on the piezoelectricity of SnSe and self-powered sensor unit driven by SnSe piezoelectric nanogenerator by a group of researchers led by Prof. Peng Li from Tsinghua University, Prof. Wanfu Shen from Tianjin University, and Prof. Dongzhi Zhang from China University of Petroleum (East China).**

A self-powered 2D-material sensor unit driven by a SnSe piezoelectric nanogenerator

2D SnSe flake demonstrates unprecedented piezoelectricity. A solely 2D-material self-powered sensor unit (SPSU) is realized by integrating a SnSe piezoelectric nanogenerator and a MoS$_2$ sensor on one chip, which demonstrates superb pH, optical and humidity sensing performance.
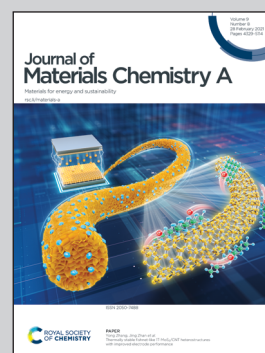
ROYAL SOCIETY OF CHEMISTRY

rsc.li/materials-a

A self-powered 2D-material sensor unit driven by a SnSe piezoelectric nanogenerator†

Peng Li, [ID] *[a] Zekun Zhang, [ID] [a] Wangtian Shen,[a] Chunguang Hu, [ID] [bc] Wanfu Shen [ID] *[bc] and Dongzhi Zhang [ID] *[d]

We report the first experimental study of the piezoelectricity of 2D SnSe crystals. SnSe demonstrates a maximum piezoelectric output voltage of ∼760 mV, which is the highest voltage generated by a single piece of 2D material reported so far. The power density reaches 28 mW m^{-2} with a mechanical-to-electrical energy conversion efficiency of 6.5%. The piezoelectricity of SnSe is highly orientation dependent, and the piezoelectric signal along the armchair orientation is ∼5 times larger than that along the zigzag orientation. A SnSe piezoelectric nanogenerator is able to monitor human body motion and vital health signs, such as the heart rate, because of its unprecedented piezoelectricity. We demonstrate a solely 2D-material self-powered sensor unit (SPSU) by integrating a SnSe nanogenerator and a MoS$_2$ multi-functional sensor on one chip. This all-in-one system powered by heartbeats and periodical bending demonstrates superb pH, illumination intensity, and humidity sensing performance. The sensing mechanism of the SPSU is investigated. The discovery of piezoelectricity in SnSe provides a way for achieving novel self-powered atomic-scale electromechanical systems which could stimulate further fundamental research and potential applications.

1. Introduction

Two-dimensional (2D) materials have drawn significant attention in both fundamental and applied research fields in recent years due to their unique electrical and mechanical properties.[1–4] Their exceptional electrical properties, extremely large surface-to-volume ratio, ultra-low noise level, and facile preparation make them promising candidates for sensing applications, including pH,[5,6] ion,[7–9] gas,[10–12] and humidity sensing.[13,14] Compared with traditional MEMS (microelectromechanical systems) sensors, 2D-material sensors have a smaller size, lower energy consumption, superior sensing performance, and better flexibility.[15,16] However, the power supply has become the bottleneck of 2D-material sensing technology. Sensors based on 2D materials reported so far rely on a macroscopic external power supply, which hinders the miniaturization of the whole sensing system. Besides, with the rapid development of the internet of things (IoT) and sensor networks, trillions of sensor units will be needed and distributed on the earth. Charging or replacing trillions of batteries with a limited life time will be an impossible work. Considering the large amount of mechanical energy that exists in an ambient environment, using piezoelectric, triboelectric, or hybridized nanogenerators is a promising way to scavenge mechanical energy[17–31] and realize self-powered 2D-material sensor units.

Piezoelectric materials allow reversible conversion between mechanical energy and electrical energy. Mechanical stress applied to these materials changes the electronic polarization, resulting in an internal electric field. Piezoelectric materials play a critical role in a rich variety of sensors, actuators, flexible electronics, and nanogenerators.[32–34] The limitation of conventional 3D piezoelectric materials, such as AlN, quartz, and PZT, arises due to their brittle nature. Additionally, the rapid growing requirement for miniaturized devices calls for low-dimensional piezoelectric materials. 1D piezoelectric materials, including ZnO nanowires,[35–37] have poor compatibility with semiconductor manufacture processes. Wu. *et al.* first reported the piezoelectric effect of monolayer MoS$_2$.[38] Since then 2D piezoelectric materials have emerged as next generation piezoelectric materials. 2D materials, such as MoS$_2$, are usually able to withstand large strain up to 11%,[39] implying that they are resistant to mechanical failure. Compared with 1D piezoelectric materials, 2D materials are more compatible with semiconductor manufacture processes because of their planar structure. To date most studies have focused on MoS$_2$. However,

[a] *State Key Laboratory of Precision Measurement Technology and Instruments, Department of Precision Instruments, Tsinghua University, Beijing 100084, China. E-mail: pengli@mail.tsinghua.edu.cn*

[b] *College of Precision Instrument and Optoelectronics Engineering, Tianjin University, Tianjin 30072, China. E-mail: swf2014@tju.edu.cn*

[c] *State Key Laboratory of Precision Measuring Technology and Instruments, Tianjin University, NO. 92 Weijin Road, CN-300072 Tianjin, China*

[d] *College of Control Science and Engineering, China University of Petroleum (East China), Qingdao 266580, China. E-mail: dzzhang@upc.edu.cn*

† Electronic supplementary information (ESI) available. See DOI: 10.1039/d0ta10457d

the piezoelectricity of monolayer MoS_2 is relatively weak with a maximum output voltage of only ∼15 mV.[38] As such, a 2D material with superb piezoelectricity is highly desired. The piezoelectricity of SnSe, which is predicted to be two orders of magnitude larger than that of monolayer MoS_2,[40] remains only theoretically explored.

In this paper, we experimentally investigated the giant in-plane piezoelectric properties of 2D SnSe crystals for the first time. SnSe flakes derived from the mechanical exfoliation method demonstrated a record high piezoelectric output voltage of ∼760 mV. SnSe crystals showed a strong anisotropic piezoelectric response, and armchair is the optimum orientation. An atomically thin nanogenerator based on SnSe was developed which matched the size of 2D-material sensors. We realized a solely 2D-material self-powered sensor unit (SPSU) by integrating the SnSe nanogenerator and a (pH, optical, and humidity) sensor based on a single MoS_2 flake on one chip without the need for a battery power source. The SPSU demonstrated superb sensing performance.

2. Experimental

2.1 SnSe synthesis and characterization

2D SnSe flakes were mechanically exfoliated by using scotch tape from bulk SnSe crystals and then transferred onto an oxygen plasma dry etching pretreated flexible poly(ethylene terephthalate) (PET) substrate. The PET substrate was heated to 80 °C for 10 min during the transferring process in order to enhance adhesion force between it and SnSe flakes. SnSe samples were identified under an optical microscope, and thin SnSe flakes were initially chosen by using an optical contrast identification approach. Their thicknesses were accurately determined by using a contact mode atomic force microscope (AFM). The crystal structure of SnSe was characterized by using a FEI Tecnai G2 20 transmission electron microscopy (TEM). The quality of the SnSe flakes was further characterized by confocal Raman microscopy with an excitation laser wavelength of 532 nm. The power of the laser was lower than 0.5 mW in order to avoid sample damage, and the acquisition times for SnSe samples were 180 s. The principal axes of SnSe flakes were determined by using a homemade azimuth-resolved reflectance difference microscope.

2.2 SnSe device fabrication and characterization

SnSe piezoelectric devices were fabricated after SnSe synthesis and characterization processes. Because SnSe flakes have macroscopic continuity, we defined metal electrodes by photolithography instead of electron beam lithography to largely reduce the fabrication cost. Sequentially, Cr (10 nm) and Au (100 nm) thin layers were deposited on the PET substrate by sputtering, followed by a metal lift-off process. The distance between the metal electrodes was 5 μm. The piezoelectric output voltage/current of the SnSe nanogenerator and the resistance of the MoS_2 sensor were measured by using a Keysight 34470A multimeter. All the measurements were carried out in an ambient environment at room temperature.

3. Results and discussion

3.1 SnSe and nanogenerator characterization

Fig. 1a and b show the photo and optical microscopy images of the SnSe device, respectively. Contact mode AFM measurements demonstrated that the lateral size of typical SnSe samples was over 10 μm, and its thickness was ∼190 nm (Fig. 1c). The van der Waals force between adjacent SnSe layers is significantly stronger than that between other 2D materials, such as MoS_2, so it is difficult to exfoliate ultrathin SnSe flakes. Fig. 1d presents the high resolution TEM image of an exfoliated SnSe sample, indicating an orthorhombic crystal structure. The single crystalline nature of SnSe flakes can be confirmed from the TEM diffraction image, as shown in Fig. 1e. Fig. 1f exhibits the Raman spectrum of a SnSe sample. Four characteristic peaks are located at 70.4 cm^{-1}, 107.0 cm^{-1}, 130.5 cm^{-1}, and 149.2 cm^{-1}, which are Raman shifts attributed to the A_g^1, B_g^2, A_g^2, and A_g^3 phonon modes of SnSe, respectively.[41] A_g^1 and A_g^3 peaks correspond to the out-of-plane vibration of atoms, whereas B_g^2 and A_g^2 correspond to in-plane vibration. The sharp Raman peaks in Fig. 1f imply that the SnSe samples studied in this work were high quality crystals.

3.2 Piezoelectricity of SnSe

We systematically investigated the piezoelectric response of SnSe. Fig. 2a shows the schematic diagram of the bending of the SnSe nanogenerator. As demonstrated in Fig. 2b, when the PET substrate was bent, SnSe attached on its surface underwent uniaxial strain with a magnitude proportional to the bending radius. Piezoelectric polarization charges of opposite polarity were generated at two edges of the SnSe flake and resulted in an output voltage peak. The reverse charge flow led to a voltage peak with an opposite sign as the substrate was released. According to our experimental results, the maximum output voltage reached 760 mV (Fig. 2b), which is ∼50 times larger than that of the MoS_2 nanogenerator reported (∼15 mV),[38] indicative of the outstanding piezoelectric properties of SnSe. This result is consistent with the theoretical prediction.[25] The magnitude of the output voltage is related to the uniaxial bending strain ε applied, which can be derived from the following equation:[42]

$$\varepsilon = h/2r \tag{1}$$

where h is the thickness of the PET substrate (150 μm), and r is the PET substrate bending radius. As illustrated in Fig. 2c, the output voltage of a typical SnSe nanogenerator was linearly proportional to the bending strain. The output voltage reached 100 mV at a strain of 0.6%. The piezoelectric output voltage also depends on the bending/releasing rate, so asymmetric output signals were observed as the bending rate was larger/smaller than the releasing rate (Fig. S1, ESI†). The periodic bending and releasing of the PET substrate led to periodic output voltage/current signals. The cycle test demonstrated that the output signal of the SnSe nanogenerator was stable over a long period of operation time (Fig. 2d). By constructively connecting two SnSe nanogenerators in series, the enhancement of the

This journal is © The Royal Society of Chemistry 2021

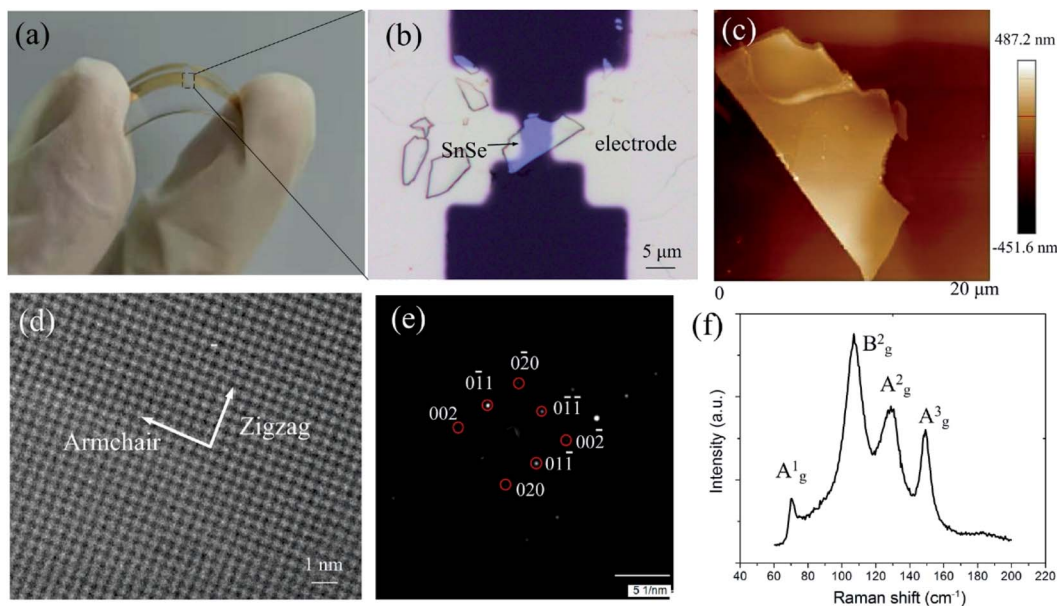*J. Mater. Chem. A*, 2021, **9**, 4716–4723 | **4717**

Fig. 1 (a) Photo of the SnSe piezoelectric device. (b) Optical microscopy image of the SnSe piezoelectric device. (c) AFM topographic image of the SnSe flake. The SnSe flake is the same one demonstrated in (b). (d) High resolution TEM image of the SnSe crystal. (e) TEM diffraction image of SnSe. (f) Raman spectrum of SnSe.

output voltages was clearly observed (Fig. S2, ESI†). By destructively connecting two devices in series, the output voltages approximately equaled the difference of the two individual output voltages. No piezoelectric output signal was observed from bare PET substrates without SnSe flakes (Fig. S3, ESI†). Fig. 2e and f show the output characteristics of a typical SnSe nanogenerator at 0.1% strain coupled to a load resistor. The output current reduced with increasing load resistance value, whereas the voltage across the load resistance changed with an opposite trend. The maximum output power of the SnSe nanogenerator reached 5.6 pW at a load resistance of ~5 MΩ (Fig. 2f). The power density reached 28 mW m^{-2}. According to our experimental results, the piezoelectric coefficient of SnSe derived is $d_{11} = 23$ pm V^{-1}. The equivalent capacitance of SnSe and the system is:[43]
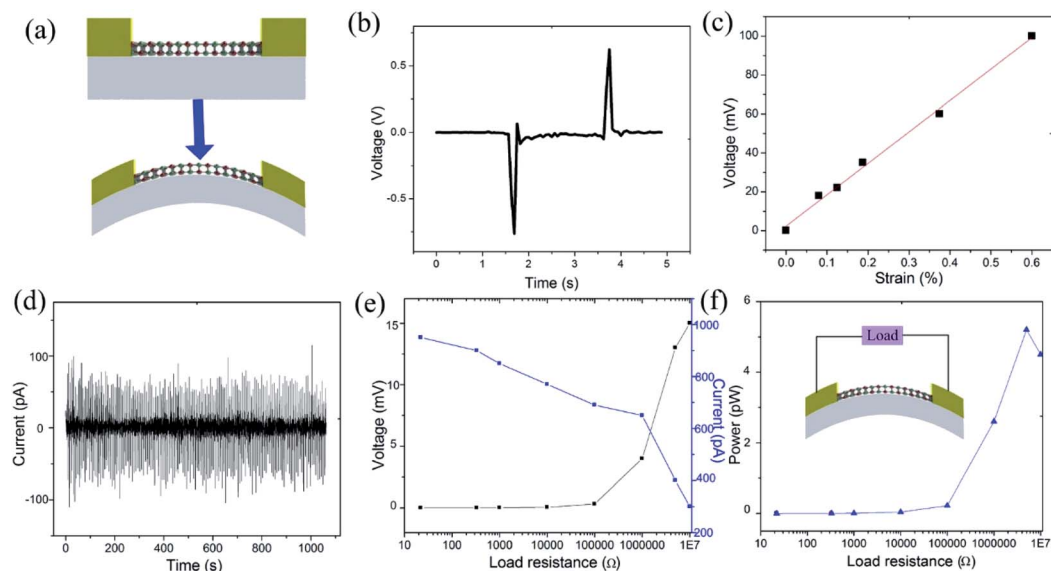

Fig. 2 (a) Schematic diagram of the bending of the SnSe nanogenerator. (b) Output voltage signal of a typical SnSe nanogenerator, which reaches 760 mV. (c) Output voltages of the SnSe nanogenerator as a function of strain. (d) Cycle test of the SnSe nanogenerator, demonstrating good stability. (e) Dependence of the output voltage and current of the SnSe nanogenerator as a function of load resistance. (f) Dependence of the output power of the SnSe nanogenerator as a function of load resistance.

4718 | J. Mater. Chem. A, 2021, 9, 4716–4723

This journal is © The Royal Society of Chemistry 2021

$$C \approx t/R \tag{2}$$

where t is the full width at half maximum of the voltage peak, and R is the equivalent resistance. The output electrical energy in one piezoelectric discharge event is:[43]

$$W_E = V^2 C/2 \tag{3}$$

where V is the peak output voltage. The mechanical energy stored in monolayer SnSe is:

$$W_M = LWE\varepsilon^2/2 \tag{4}$$

where L and W are the length and width of SnSe, respectively, and E is the Young's modulus of SnSe. The efficiency of converting mechanical energy to electrical energy is:

$$\eta = W_E/W_M \tag{5}$$

According to our experimental results, $\eta \approx 6.5\%$. SnSe is a good thermoelectric material upon doping. However, we assume that doped SnSe which becomes electrically conductive will not be piezoelectric, and piezoelectric voltage/current will not be generated upon bending.

The dependence of the piezoelectric response of SnSe on the crystal orientation was investigated. We used azimuth-resolved reflectance difference microscopy (ADRDM), a nondestructive approach, to identify the two orthogonal principal axes (armchair and zigzag) of anisotropy SnSe crystals. ADRDM measures the normalized reflectance difference $N(\theta)$ of two polarized light, s and p, while regulating the incident directions of linearly polarized light. The $N(\theta)$ value can be derived from the following equation:[44,45]

$$N(\theta) = \frac{(R_s - R_p)}{R_s + R_p} \cos 2(\theta - \theta_0) \tag{6}$$

where R_s and R_p are the reflectance of s and p polarized light, respectively, θ is the azimuthal angle of the incident light, and θ_0 represents one of the crystalline axes of the sample. $N(\theta)$ reaches extreme values when the incident polarization direction matches the armchair or zigzag orientations of the SnSe crystal. More details of the ADRDM setup were described in our previous reports.[44,45] Fig. 3b demonstrates that $N(\theta)$ derived from the center spot of a typical SnSe flake achieved the maximum and minimum values at 51° and 141°, respectively, which correspond to the directions of the two principal axes. ADRDM can also serve as an imaging tool capable of measuring $N(\theta)$ at all pixels inside the field of view and create anisotropy contrast images. Fig. 3c displays the ADRDM images of the same SnSe flake taken at different azimuth angles with $N(\theta)$ shown on a color scale. It should be noted that the optical microscope image (Fig. 3a) and ADRDM images (Fig. 3c) are symmetric as mirror images. The SnSe flake in the same ADRDM image showed the same color, indicating an identical orientation and single crystalline structure. In order to further distinguish between the armchair and zigzag orientations, we measured the electrical properties of SnSe by fabricating two

pairs of metal electrodes on target SnSe flakes along the two orthogonal principal axes determined by ADRDM (Fig. 3d). The I–V measurements showed that the electrical properties were highly anisotropic (Fig. S4, ESI†). According to Yang *et al.*, SnSe exhibits the highest and lowest conductivity along armchair and zigzag directions, respectively.[41] Therefore, the orientations of SnSe were precisely identified by ADRDM along with anisotropic electrical measurements. The output voltages of the SnSe nanogenerator at 0.1% strain along the armchair direction were ~5 times larger than that along the zigzag direction (Fig. 3e), indicating strong anisotropic piezoelectric properties. Mechanical stress applied to the material changes the electronic polarization which results in piezoelectricity. In SnSe crystals, the mirror symmetry along the zigzag direction still remains under a uniaxial strain, which indicates that the electronic polarization change is negligible and piezoelectricity along this direction is very weak. Therefore, armchair is the optimum orientation for SnSe piezoelectric devices.

3.3 Energy harvesting from the human body

Fig. 4a displays energy harvesting from finger bending by attaching the nanogenerator to the tester's index finger joint. The output signals clearly enhanced as the bending degree increased from 30° to 90°. Output voltage signals were also observed as the device was attached on the tester's wrist (Fig. 4b), knee (Fig. 4c), elbow (Fig. S5a, ESI†), and neck (Fig. S5b, ESI†) with signal magnitudes proportional to bending angles. Therefore, the SnSe piezoelectric device holds great potential in human activity monitoring. The SnSe nanogenerator was then attached to the neck to noninvasively monitor muscle movement during speech (Fig. 4d). The obtained V–t curves were clearly different when the tester pronounced different words, such as "hello", "nano", and "happy". The waveforms illustrated similar characteristic peaks when the tester spoke the same word, indicating good repeatability. It brings promise for remote control of human/machine interfaces. Next, we demonstrated prototype wearable SnSe derives that are capable of noninvasively monitoring vital health signs, such as the heart rate. Due to the remarkable piezoelectric properties, the SnSe nanogenerator could be applied as a pulse detector by attaching it around the wrist (Fig. 4e). The magnitude of the output voltages was ~0.3 mV. The SnSe nanogenerator can also successfully convert the mechanical energy from heartbeats into electric power by attaching it on the chest of the tester (Fig. 4f). The magnitude of the output signal was ~1.2 mV, and the heart rate extracted (~90/min) was consistent with the measurement by a SnSe nanogenerator pulse detector (Fig. 4e). Therefore, SnSe piezoelectric devices hold great potential in health-tracking wearable devices.

3.4 Solely 2D-material self-powered sensor unit

After demonstrating SnSe nanogenerator's remarkable electromechanical conversion ability, we tried to use the nanogenerator to drive a 2D-material sensor. As a proof of concept, a SnSe nanogenerator and a MoS_2 sensor were integrated on a flexible PET substrate. They were connected in series to form
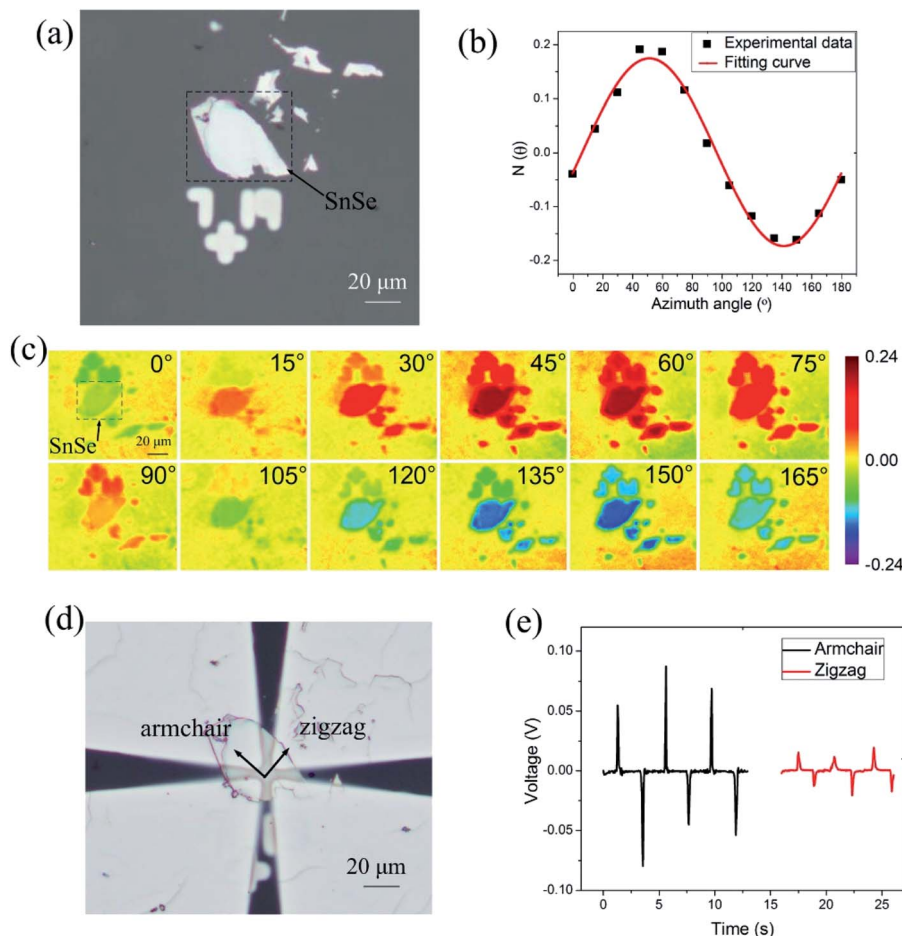
Fig. 3 (a) Optical microscopy image of a SnSe flake. (b) $N(\theta)$ derived from the center spot of the SnSe flake in (a). $N(\theta)$ reaches maximum and minimum values at 51° and 141°, respectively, which correspond to the directions of two principal axes. (c) ADRDM images of the SnSe flake in taken at different azimuth angles with $N(\theta)$ shown on a color scale. (d) Optical microscope image of a SnSe device with two pairs of orthogonal electrodes whose directions are parallel to zigzag and armchair directions, respectively. The SnSe flake is the same one demonstrated in (a). (e) Piezoelectric properties of SnSe along armchair/zigzag directions.

a loop (Fig. 5a). Fig. 5b shows the optical microscopy image of the MoS_2 sensor. The thickness of the MoS_2 flake measured by AFM is ~20 nm. The Raman spectrum of MoS_2 as illustrated in Fig. 5c demonstrates two prominent characteristic peaks at 383.6 cm^{-1} and 408.7 cm^{-1}, which are Raman shifts attributed to the E_g^2 and A_g^1 phonon modes of MoS_2, respectively.[46,47] The E_g^2 peak corresponds to the in-plane vibration of atoms, whereas the A_g^1 peak corresponds to out-of-plane vibration. The gap between the two peaks, 25.1 cm^{-1}, indicates few-layer MoS_2.

We then demonstrated a self-powered MoS_2 pH sensor driven by the SnSe nanogenerator. Solutions with different pH values were sequentially introduced onto the MoS_2 sensor at room temperature. The resistance of the MoS_2 sensor significantly decreased as the pH value changed from 9.2 to 4.0. This process was repeated several times and demonstrated good repeatability (Fig. 5d). The response and recovery rate of our MoS_2 sensor extracted were both less than 5 s. This fast response is mainly attribute to the superb electrical properties and large surface-volume ratio of MoS_2. The pH sensing mechanism of the MoS_2 sensor was investigated. The I–V curve

of a typical MoS_2 device demonstrates good linearity (Fig. S6, ESI†), indicating an insignificant Schottky barrier between MoS_2 and Cr/Au metal electrodes.[48] Therefore, the influence of MoS_2/metal contact resistance is negligible and the output signals are mainly attributed to the response of the MoS_2 flake during sensing. The gating effect due to the adsorption of H$^+$ or OH$^-$ ions on the surface of the MoS_2 flake drastically changes its carrier density and carrier mobility, resulting in MoS_2 resistance variation. The equation, $\rho = 1/nq\mu$, demonstrates this relationship clearly, where ρ is the resistivity of MoS_2, n is the carrier density, q is the charge per carrier, and μ is the carrier mobility. By driving the MoS_2 pH sensor with the SnSe nanogenerator, a clear sensitivity to pH change was observed (Fig. 5e). The voltage signal across the MoS_2 sensor increased from ~0.1 mV to ~0.6 mV as the pH value varied from 2.0 to 12.0 inasmuch as the resistance of MoS_2 drastically increased. In addition to periodic bending of the substrate, we also tried to use heartbeats as the energy source to operate the SPSU by attaching it on the chest of a tester. The voltage across the MoS_2 sensor demonstrated the same trend of variation as the pH

4720 | *J. Mater. Chem. A*, 2021, **9**, 4716–4723

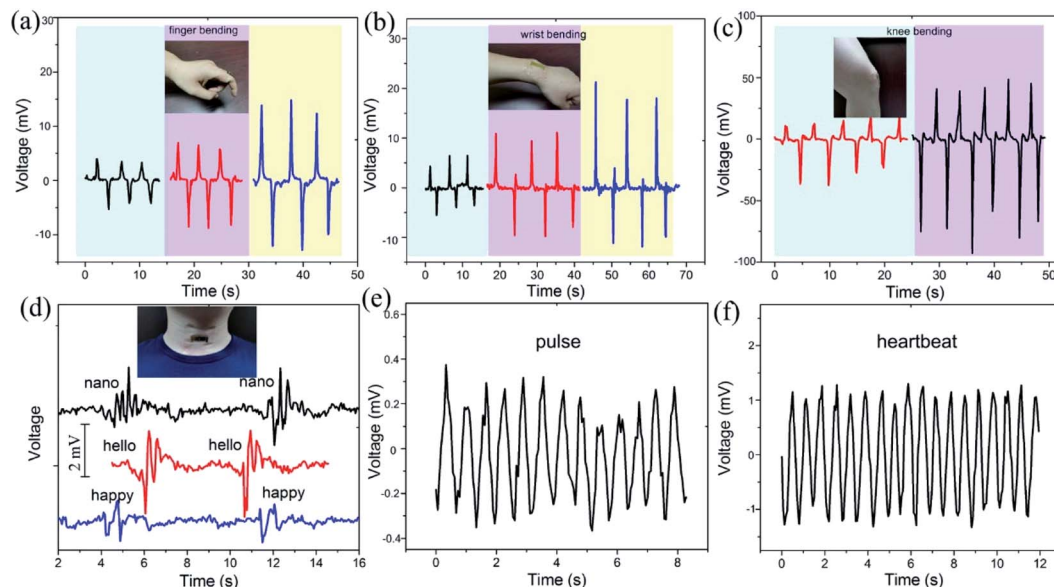This journal is © The Royal Society of Chemistry 2021

Fig. 4 Energy harvesting of the SnSe nanogenerator from a finger joint (a), wrist (b), and knee (c), respectively. The signal magnitudes are proportional to the bending angles. (d) Muscle movement during speech detected by attaching the SnSe nanogenerator to the neck. $V-t$ curves were clearly different when the tester pronounced different words, such as "hello", "nano", and "happy". (e) Pulse rate detection by attaching the SnSe nanogenerator on the wrist. (f) Heart rate detection by attaching the SnSe nanogenerator on the chest of the tester.

value increased (Fig. 5f). Therefore, the SPSU can effectively monitor the pH value and holds great potential for self-powered electronic tongue applications.

The SnSe nanogenerator was also used to power a MoS_2 photodetector. We utilized a white light source to illuminate the MoS_2 sensor, and the optical power distributed on the MoS_2 channel was ~0.2 mW. The resistance of MoS_2 rapidly reduced

from 420 kΩ to 240 kΩ within 10 s. After the light was turned off, the resistance gradually changed back to the original value in 50 s. This process was repeated seven times and demonstrated good repeatability (Fig. 6a). The photoresponsivity of the MoS_2 sensor extracted was 9 mA W^{-1}. Without illumination, MoS_2 is in its equilibrium state. Illumination results in photon absorption and the excitation of electron–hole pairs, which can
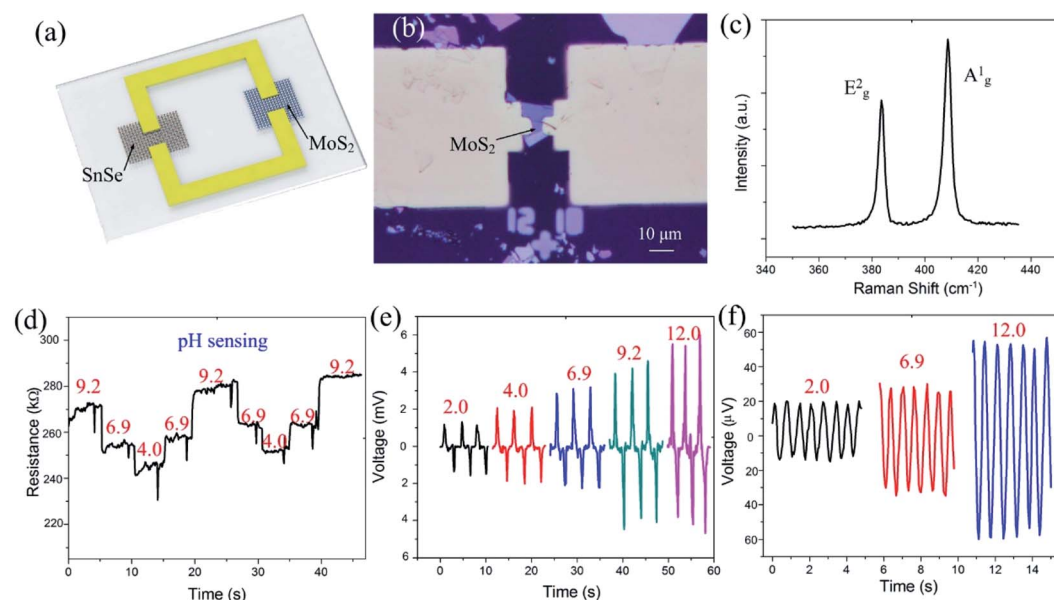

Fig. 5 (a) Schematic view of the SnSe nanogenerator integrated with a MoS_2 sensor. (b) Optical microscopy image of the MoS_2 sensor. (c) Raman spectrum of MoS_2. (d) Dynamic resistance variation of the MoS_2 pH sensor as the pH value changes from 9.2 to 4.0. (e) The pH sensing performance of the SPSU upon periodic bending of the substrate. (f) The pH sensing performance of the SPSU by using heartbeats as the energy source.
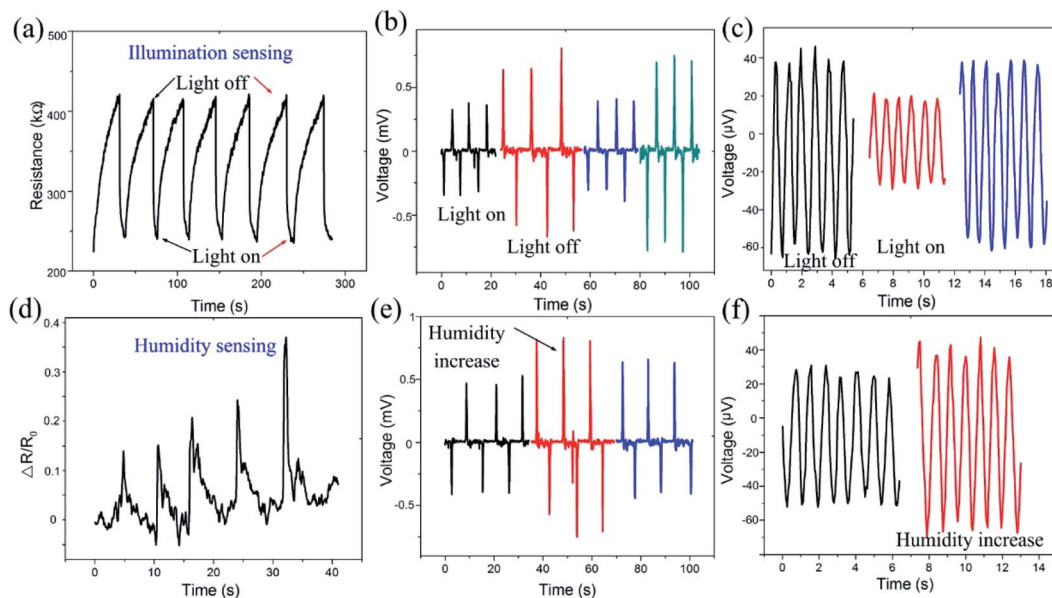
Fig. 6 (a) Dynamic resistance variation of the MoS_2 photodetector. (b) Illumination sensing performance of the SPSU upon periodic bending of the substrate. (c) Illumination sensing performance of the SPSU by using heartbeats as the energy source. (d) Dynamic resistance variation of the MoS_2 humidity sensor. The resistance of MoS_2 significantly increases as the fingertip approaches the sensor which increases the local humidity. When the fingertip moved far away from the sensor, the resistance of MoS_2 reduced back to the original value. (e) Humidity sensing performance of the SPSU by periodic bending of the substrate. The distance between the fingertip and MoS_2 sensor is 5 mm. (f) Humidity sensing performance of the SPSU by using heartbeats as the energy source. The distance between the fingertip and MoS_2 sensor is 5 mm.

be extracted by applying a bias. As a result, MoS_2 converts the energy of photons absorbed into photocurrent, and its conductivity increases accordingly. By driving the MoS_2 photodetector with the SnSe nanogenerator, a clear sensitivity to illumination change was observed (Fig. 6b). The voltages across the MoS_2 sensor decreased from ~0.7 mV to ~0.4 mV after the light was turned on. The photoresponsivity of the SPNS extracted was 1.5 V W^{-1}. In addition to periodic bending of the substrate, we tried to use heartbeats (Fig. 6c) and pulses (Fig. S7, ESI†) to power the SPSU, respectively. After illumination, the voltage across the MoS_2 sensor reduced from ~60 μV to ~30 μV, and from ~20 μV to ~10 μV, respectively. Therefore, the SPNS can effectively monitor illumination intensity and holds great potential for self-powered photoelectric devices.

We finally demonstrated a self-powered MoS_2 humidity sensor driven by a SnSe nanogenerator. We used a fingertip as a moist source to approach the sensor to increase local humidity and simultaneously recorded the resistance variation of MoS_2 at room temperature. The environmental humidity value was below 20%. Water molecules adsorbed on the MoS_2 surface drastically change the carrier density n and carrier mobility μ, and thus the resistivity of MoS_2 flakes. In Fig. 6d, the dynamic response of the MoS_2 sensor demonstrated 5 peaks which correspond to 5 different distances between the fingertip and the MoS_2 sensor (from 12 mm to 4 mm). A smaller distance resulted in a higher peak. When the fingertip moved far away from the sensor, the local humidity value decreased and the resistance of MoS_2 rapidly reduced back to the original value. In order to figure out whether the local temperature change is also a major factor that causes the resistance variation when the fingertip approaches the MoS_2 sensor, we used a heat source

whose temperature was ~40 °C to move close to MoS_2. As a result, the sensor showed a negligible response ($\Delta R/R_0 < 0.05$, Fig. S8, ESI†). Fig. 6e displays the performance of the MoS_2 humidity sensor powered by the SnSe nanogenerator. The voltage across the MoS_2 sensor varied from ~0.6 mV to ~0.8 mV when the fingertip approached the sensor with a distance of 5 mm. We then tried to use heartbeats to power the SPSU by attaching it on the chest of a tester, and the output voltages across the MoS_2 sensor varied from ~30 μV to ~50 μV when the fingertip moved close to the MoS_2 sensor (Fig. 6f). Therefore, the SPSU has good humidity sensing performance and holds great potential for self-powered electronic skin applications.

4. Conclusions

The remarkable in-plane piezoelectric properties of 2D SnSe crystals were experimentally investigated for the first time and were found to be highly orientation dependent. We integrated a SnSe nanogenerator and MoS_2 multi-functional sensor on one chip. This all-in-one system which was powered by heartbeats and periodical bending holds great potential in many application fields, such as electronic tongues, electronic skin, and photoelectric devices. Our research provides a platform for fundamental investigation of electronic polarization and electromechanical conversion in 2D piezoelectric materials and provides a route for achieving novel self-powered atomic-scale electromechanical systems.

Conflicts of interest

The authors declare no conflict of interest.

4722 | *J. Mater. Chem. A*, 2021, **9**, 4716–4723

This journal is © The Royal Society of Chemistry 2021

Acknowledgements

References

1 Y. Zhang, T. T. Tang, C. Girit, Z. Hao, M. C. Martin, A. Zettl, M. F. Crommie, Y. R. Shen and F. Wang, *Nature*, 2009, **459**, 820.

2 C. Lee, X. D. Wei, J. W. Kysar and J. Hone, *Science*, 2008, **312**, 385–388.

3 Z. Huang, Z. W. Han, H. Tang, L. Ren, D. S. Chander, X. Qi and H. Zhang, *2D Mater*, 2015, **2**, 035011.

4 E. Cha, M. D. Patel, J. Park, J. Hwang, V. Prasad, K. Cho and W. Choi, *Nat. Nanotechnol.*, 2018, **13**, 337.

5 Y. Ohno, K. Maehashi, Y. Yamashiro and K. Matsumoto, *Nano Lett.*, 2009, **9**, 3318–3322.

6 P. K. Ang, W. Chen, A. T. S. Wee and K. P. Loh, *J. Am. Chem. Soc.*, 2008, **130**, 14392.

7 T. Kuila, S. Bose, P. Khanra, A. K. Mishra, N. H. Kim and J. H. Lee, *Biosens. Bioelectron.*, 2011, **26**, 4637–4648.

8 A. Maity, A. X. Sui, H. Pu, K. J. Bottum, B. Jin, J. Chang, G. Zhou, G. Lu and J. Chen, *Nanoscale*, 2020, **12**, 1500–1512.

9 P. Li, D. Zhang, J. Liu, H. Chang, Y. Sun and N. Yin, *ACS Appl. Mater. Interfaces*, 2015, **7**, 24396–24402.

10 K. Lee, R. Gatensby, N. McEvoy, T. Hallam and G. S. Duesberg, *Adv. Mater.*, 2013, **25**, 6699–6702.

11 Z. Liu, J. Huang, Q. Wang, J. Zhou, J. Ye, X. Li, Y. Geng, Z. Liang, Y. Du and X. Tian, *Sens. Actuators, B*, 2020, **308**, 127650.

12 D. Zhang, Z. Yang, P. Li, M. Pang and Q. Xue, *Nano Energy*, 2019, **65**, 103974.

13 J. Zhao, N. Li, H. Yu, Z. Wei, M. Liao, P. Chen, S. Wang, D. Shi, Q. Sun and G. Zang, *Adv. Mater.*, 2017, **29**, 1702076.

14 D. J. Late, Y. K. Huang, B. Liu, J. Acharya, S. N. Shirodkar, J. J. Luo, A. M. Yan, D. Charles, U. V. Waghmare, V. P. Dravid and C. N. R. Rao, *ACS Nano*, 2013, **7**, 4879–4891.

15 J. H. Kim, A. Mirzaei, H. W. Kim and S. S. Kim, *Sens. Actuators, B*, 2020, **313**, 128040.

16 Q. He, Z. Zeng, Z. Yin, H. Li, X. Wu, X. Huang and H. Zhang, *Small*, 2012, **8**, 2994–2999.

17 K. Zhang, S. Wang and Y. Yang, *Adv. Energy Mater.*, 2017, **7**, 1601852.

18 X. Wang and Y. Yang, *Nano Energy*, 2017, **32**, 36–41.

19 Y. Su, Y. Yang, X. Zhong, H. Zhang, Z. Wu, Y. Jiang and Z. L. Wang, *ACS Appl. Mater. Interfaces*, 2014, **6**, 553–559.

20 Y. Wu, X. Wang, Y. Yang and Z. L. Wang, *Nano Energy*, 2015, **11**, 162–170.

21 Y. Ji, K. Zhang and Y. Yang, *Adv. Sci.*, 2018, **5**, 1700622.

22 K. Zhang, Z. L. Wang and Y. Yang, *ACS Nano*, 2016, **10**, 4728–4734.

23 D. Zhang, Y. Wang and Y. Yang, *Small*, 2019, **15**, 1805241.

24 K. Zhao, Y. Wang, L. Han, Y. Wang, X. Luo, Z. Zhang and Y. Yang, *Nano-Micro Lett.*, 2019, **11**, 19.

25 K. Zhang, Y. Wang, Z. L. Wang and Y. Yang, *Nano Energy*, 2019, **55**, 534–540.

26 K. Zhao, B. Ouyang, C. R. Bowen and Z. L. Wang, *Nano Energy*, 2020, **71**, 104632.

27 Y. Jiang, Y. Wang, H. Wu, Y. Wang, R. Zhang, H. Olin and Y. Yang, *Nano-Micro Lett.*, 2019, **11**, 99.

28 K. Zhang, Y. Wang and Y. Yang, *Adv. Funct. Mater.*, 2019, **29**, 1806435.

29 M. A. Johar, A. Wasee, M. A. Hassan, I. V. Bagal, A. Abdullah, J. S. Ha and S. W. Ryn, *Adv. Energy Mater.*, 2020, 2002608.

30 X. R. Zhou, K. Parida, O. Halevi, Y. Z. Liu, J. Q. Xiong, S. Magdassi and P. S. Lee, *Nano Energy*, 2020, 104676.

31 H. Khan, N. Mahmood, A. Zavabeti, A. Elbourne, M. A. Rahman, B. Y. Zhang, V. Krishnamurthi, P. Atkin, M. B. Ghasemian, J. Yang, G. L. Zheng, A. R. Ravindran, S. Walia, L. Wang, S. P. Russo, T. Daeneke, Y. X. Li and K. Kalantar-Zadeh, *Nat. Commun.*, 2020, **11**, 3449.

32 F. Yang, J. Guo, L. Zhao, W. Shang, Y. Gao, S. Zhang, G. Gu, B. Zhang, P. Cui, G. Cheng and Z. Du, *Nano Energy*, 2020, **67**, 104210.

33 Z. L. Wang, *ACS Nano*, 2013, **7**, 9533–9557.

34 X. Zhou, K. Parida, O. Halevi, Y. Liu, J. Xiong, X. Magdassi and P. S. Lee, *Nano Energy*, 2020, **72**, 104676.

35 A. T. Le, M. Ahmadipour and S. Y. Pung, *J. Alloys Compd.*, 2020, **844**, 156172.

36 X. Pu, J. W. Zha, C. L. Zhao, S. B. Gong, J. F. Gao and R. K. Y. Li, *Chem. Eng. J.*, 2020, **398**, 125526.

37 R. Sahoo, S. Mishra, L. Unnikrishnan, S. Mohanty, S. Mahapatra, S. K. Nayak, S. Anwar and A. Ramadoss, *Mater. Sci. Semicond. Process.*, 2020, **117**, 105173.

38 W. Wu, L. Wang, Y. Li, F. Zhang, L. Lin, S. Niu, D. Chenet, X. Zhang, Y. Hao, T. F. Heinz, J. Hone and Z. L. Wang, *Nature*, 2014, **514**, 470.

39 S. Bertolazzi, J. Brivio and A. Kis, *ACS Nano*, 2011, **5**, 9703–9709.

40 R. Fei, W. Li, J. Li and L. Yang, *Appl. Phys. Lett.*, 2015, **107**, 173104.

41 S. Yang, Y. Liu, M. Wu, L. D. Zhao, Z. Lin, H. C. Cheng, Y. Wang, C. Jiang, S. H. Wei, L. Huang, Y. Huang and X. Duan, *Nano Res.*, 2018, **11**, 554.

42 P. Li, D. Zhang, J. Wu, Y. Cao and Z. Wu, *Sens. Actuators, B*, 2018, **273**, 358–364.

43 Z. L. Wang and J. Song, *Science*, 2006, **312**, 242–246.

44 S. Yang, C. Hu, M. Wu, W. Shen, S. Tongay, K. Wu, B. Wei, Z. Sun, C. Jiang, L. Huang and Z. Wang, *ACS Nano*, 2018, **12**, 8798–8807.

45 W. Shen, C. Hu, J. Tao, J. Liu, S. Fan, Y. Wei, C. An, J. Chen, S. Wu, Y. Li, J. Liu, D. Zhang, L. Sun and X. Hu, *Nanoscale*, 2018, **10**, 8329–8337.

46 H. Li, Q. Zhang, C. C. R. Yap, B. K. Tay, T. H. T. Edwin, A. Olivier and D. Baillargeat, *Adv. Funct. Mater.*, 2012, **22**, 1385–1390.

47 Y. Zhan, Z. Liu, S. Najmaei, P. M. Ajayan and J. Lou, *Small*, 2012, **8**, 966–971.

48 S. McDonnell, R. Addou, C. Buie, R. M. Wallace and C. L. Hinkle, *ACS Nano*, 2014, **8**, 2880.

This journal is © The Royal Society of Chemistry 2021

J. Mater. Chem. A, 2021, **9**, 4716–4723 | **4723**